



# Core-shell structured nanoprecipitates in zirconium based alloy

Chengze Liu <sup>a, b</sup>, Geping Li <sup>a,\*</sup>, Fusen Yuan <sup>a,b</sup>, Fuzhou Han <sup>a,b</sup>, Muhammad Ali <sup>a,b</sup>,  
Yingdong Zhang <sup>a,b</sup>, Wenbin Guo <sup>a,b</sup>, Hengfei Gu <sup>a,c</sup>

<sup>a</sup> Institute of Metal Research, Chinese Academy of Sciences, 72 Wenhua Road, Shenyang 110016, People's Republic of China

<sup>b</sup> School of Materials Science and Engineering, University of Science and Technology of China, 96 JinZhai Road, Baohe District, Hefei, Anhui 230026, People's Republic of China

<sup>c</sup> University of Chinese Academy of Sciences, 19 Yuquan Road, Beijing, 100049, People's Republic of China

## ARTICLE INFO

### Article history:

Received 30 January 2020

Revised 23 March 2020

Accepted 23 March 2020

### Keywords:

Precipitation

Crystal defects

Core-shell structure

Grain interfaces

## ABSTRACT

Unique precipitations with core-shell structure between metal and intermetallics were firstly observed in zirconium based alloy. The spherical core structure was identified as tetragonal  $Zr_3Ge$  nanoprecipitate, and the shell structure was determined to be face-centered-cubic (FCC) zirconium phase, which uniformly encircled the  $Zr_3Ge$  nanoparticle while obeying the orientation relationship with the hexagonal-close-packed (HCP) zirconium phase matrix:  $[1\bar{1}0]_{FCC} // [2\bar{1}\bar{1}0]_{HCP}$  and  $(1\bar{1}1)_{FCC} // (0001)_{HCP}$ . Based on electron microscopy characterization and theoretical analysis, the formation mechanism of the core-shell structured nanoprecipitates was proposed.

© 2020 Acta Materialia Inc. Published by Elsevier Ltd. All rights reserved.

Precipitation hardening has been widely implemented in metallic structural materials, such as Aluminum, Magnesium, Nickel, Titanium and Zirconium alloys. These strengthening particles of dissimilar compositions or crystalline structures impede the movement of dislocations or other defects in the crystal's lattice. Meanwhile, extra interfaces were produced, which actually act similarly as grain boundaries. For example, it was firstly observed in Al-Li-Zr alloy that  $Al_3Zr$  precipitates can serve as heterogeneous nucleation/growth sites for  $Al_3Li$  phase, resulting in a 'composite' precipitation [1]. This phenomenon has attracted wide attentions from researchers, for the superior mechanical performance at high temperatures due to core-shell precipitates [2–4], and they concluded that these precipitations were due to the segregation of alloying elements at the interface between the matrix and the pre-existed precipitates.

In this research, we report another kind of core-shell structured precipitation in a zirconium based metallic material. Using transmission electron microscope combined with spectroscopy and diffraction techniques, we have investigated the crystallographic orientation relationships among the matrix, shell structure and the nanoparticle. Furthermore, the formation mechanism of the shell structure was discussed.

The studied material, Zr-0.10%Cr-0.21%Fe-0.50%Ge-1.28%Sn-0.14%O (in weight percentage) alloy was prepared by arc melting. Subsequently, the alloy button was solid solution treated at 1100°C in furnace with a holding time of 1h, followed by isothermal forging in reduction of 50% at 1000°C, which was above the  $(\alpha+\beta)/\beta$  transus temperature, and air cooling.

As shown in Fig. 1, identification of the nanoparticle was accomplished through indexing the corresponding selected area electron diffraction (SAED) patterns and an energy dispersive spectrometer (EDS) analysis. It was concluded that the core structure was  $Zr_3Ge$  phase ( $P4_2/n$ ,  $a=b=11.07\text{\AA}$ ,  $c=5.47\text{\AA}$ ). Interestingly, a uniform shell structure with ~25nm in thickness was perfectly encircling the nanoparticle, and it did not display any segregation of alloying elements (EDS analysis referring to point B in Fig. 1).

Based on SEAD analysis (as shown in Fig. S1 in the supplementary material), the shell structure was indexed as face centered cubic (FCC) Zr ( $Fm\bar{3}m$ ,  $a=4.93\text{\AA}$ , measured by SAED patterns), obeying the orientation relationship:  $[2\bar{1}\bar{1}0]_{HCP-Zr} // [1\bar{1}0]_{FCC-Zr} // [0\bar{3}4]_{Zr_3Ge}$  and  $(0001)_{HCP-Zr} // (1\bar{1}1)_{FCC-Zr} // (\bar{1}84\bar{3})_{Zr_3Ge}$ . As shown in Fig. 2, a stacking faults region with 10nm in width was observed between the shell structure and the matrix (Fig. 2 b and f).

The HCP to FCC phase transformation has been recently observed in Ti, Zr, and Hf under straining conditions [5–10]. This transformation typically produces two types of orientation relationships between the two structures, named by B-type and P-type [7] relations, correspondingly: (1)  $[2\bar{1}\bar{1}0]_{HCP-Zr} // [1\bar{1}0]_{FCC-Zr}$

\* Corresponding author.

E-mail address: [gpli@imr.ac.cn](mailto:gpli@imr.ac.cn) (G. Li).

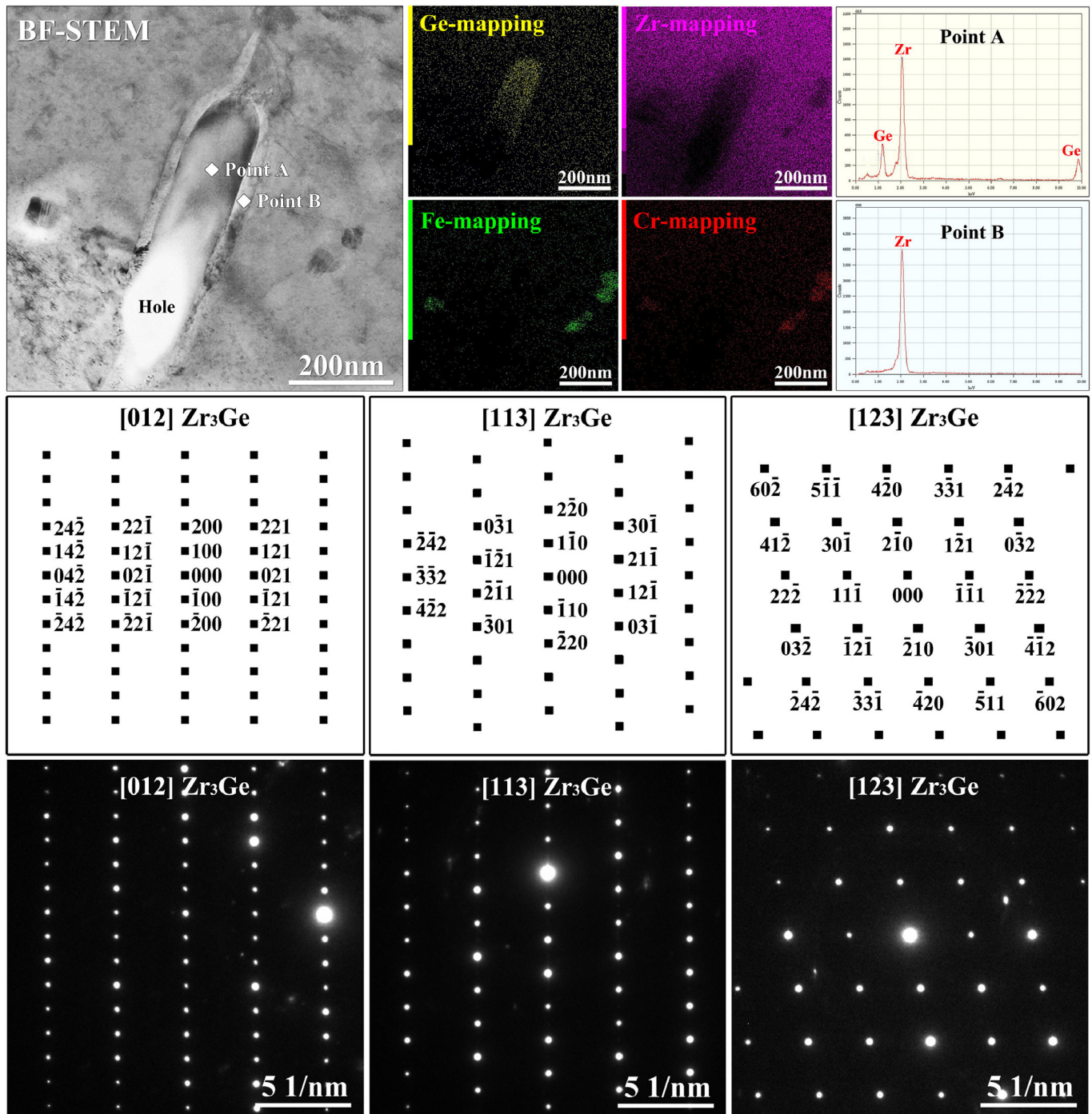


Fig. 1. EDS analysis of the region containing the core-shell structured precipitate and indexed SAED patterns of the core structure.

and  $(0001)_{\text{hcp-Zr}} \parallel (1\bar{1}1)_{\text{fcc-Zr}}$ ; (2)  $[0001]_{\text{hcp-Zr}} \parallel [0\ 0\ 1]_{\text{fcc-Zr}}$  and  $(10\bar{1}0)_{\text{hcp-Zr}} \parallel (220)_{\text{fcc-Zr}}$ . Obviously, the shell structure and matrix obeyed B-type orientation relationship. The B-type HCP-FCC transformation was mainly driven by Shockley partial dislocations with Burgers vectors of the  $1/3\langle 10\bar{1}0 \rangle$  type, which were generated and glided on every other  $(0001)_{\text{hcp-Zr}}$  plane during transformation [7]. During this transformation, the process of ...ABABABAB... sequence converting to ...ABCABCAB... required shifting of sequences in at least four crystal planes (layers), as marked by underlines. However, in earlier researches, only partial dislocations were observed

at the HCP/FCC interface, instead of a stacking faults region. Thus, the interface between the FCC shell structure and HCP matrix was further analyzed.

The interplanar spacing along the  $[0001]_{\text{hcp-Zr}}$  direction in the matrix and shell structure were different:  $2.79\text{\AA}$  for  $(0001)_{\text{hcp-Zr}}$  increased to  $2.85\text{\AA}$  for  $(1\bar{1}1)_{\text{fcc-Zr}}$ , corresponding to a transformation strain of 2.15%. As a result, the HCP matrix was subjected to an effective tension along the  $[0001]_{\text{hcp-Zr}}$  direction during the HCP to FCC transformation. Once the FCC shell structure formed, it changed the local strain distribution due to the crystal expan-

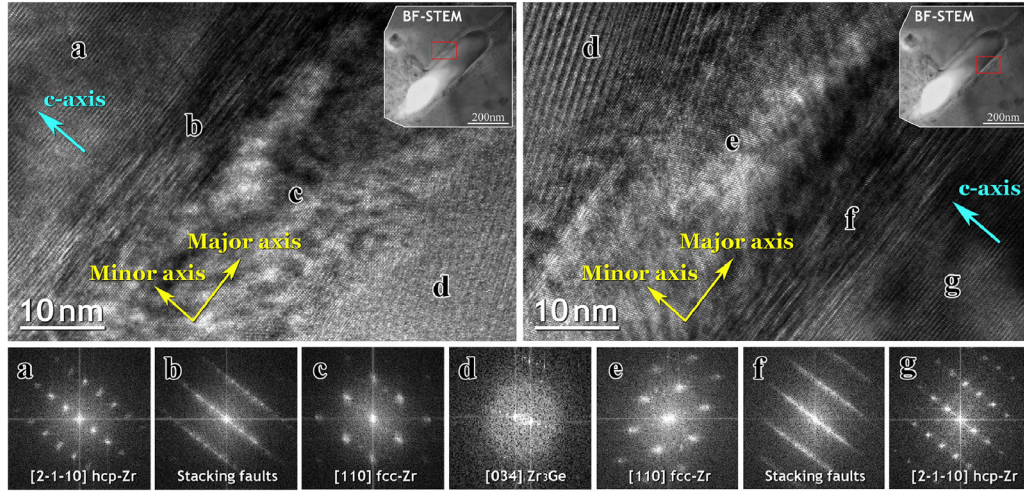


Fig. 2. HR-TEM micrograph and FFT analysis of the core-shell structured precipitate interface region viewed along  $[2\bar{1}\bar{1}0]_{\text{hcp-Zr}}$  zone axis.

sion [11]. With the help of geometric phase analysis (GPA), quantitative strain maps at the region containing the matrix, stacking faults region and shell structure were generated and analyzed. The local strain components ( $\varepsilon_{xx}$  and  $\varepsilon_{yy}$ ) were calculated by analyzing the derivative of two-dimensional displacement field, based on HR-TEM images [12]. The region marked by yellow frame in Fig. 3 (e) was defined as a reference region with zero strain. We found that there was large strain along the X direction in the stacking faults region, which was also portrayed in the horizontal intensity linescans results (Fig. 3 g). However, enervate strains along Y direction were detected (Fig. 3 h). As discussed above, the B-type transformation was driven by gliding of partial dislocations along  $(0001)_{\text{hcp-Zr}}$  planes in the matrix, resulting in the shifting of planar sequences along the  $[0001]_{\text{hcp-Zr}}$  direction. In other words, during the HCP-FCC transformation, the atomic distances along the Y direction did not alter. Thus, the  $\varepsilon_{yy}$  strain at the transition zones (the stacking faults region) between the two structures was much less than the  $\varepsilon_{xx}$  values. According to a first-principles study of stacking faults in HCP metals, the stacking fault energy (SFE) of the  $(0001)_{\text{hcp-Zr}}$  plane was lower among the close-packed crystal planes in HCP-Zr [13]. In other words, stacking faults were preferentially observed among basal planes. In this research, the faulted crystal planes in the stacking faults region were parallel to both  $(0001)_{\text{hcp-Zr}}$  and  $(1\bar{1}1)_{\text{fcc-Zr}}$  planes, which was in perfectly agreement with the theoretical calculations. In other words, the relatively low stacking fault energy had promoted the B-type HCP-FCC structure transformation and the stacking faults region. For the interface between FCC-Zr and  $\text{Zr}_3\text{Ge}$  precipitate, the interfacial structure was highly incoherent:  $[1\bar{1}0]_{\text{fcc-Zr}} \parallel [0\bar{3}4]_{\text{Zr}_3\text{Ge}}$  and  $(1\bar{1}1)_{\text{fcc-Zr}} \parallel (\bar{1}84\bar{3})_{\text{Zr}_3\text{Ge}}$ , which failed to activate a group of parallel partial dislocations. Thus, no stacking faults region were observed between the FCC-Zr and  $\text{Zr}_3\text{Ge}$  phase.

Based on TEM characterization for multiple specimens, the core-shell precipitates were only observed at grain boundaries (as shown in Figure S2 and S3 in the supplementary material). Till now, FCC-Zr phase observed in the interior were all resulted from plastic deformation at room temperature [5–11], which produces the driving force for the HCP-FCC phase transformation. In this research, the alloy went through isothermal forging followed by air cooling, which failed to provide driving force for intracrystalline

HCP-FCC phase transformation. According to our research [14], the dragging force between nanoprecipitates and grain boundary could lead to phase transformations in zirconium alloy. Thus, the grain boundary dragging effect could be one of the prerequisites for the core-shell structured precipitates. As shown in Fig. 4 (a), the grain boundary near the nanoparticle was curved due to the pinning effect. As a result, dragging force ( $F$ ) was applied to the nanoparticle and it could be calculated by:

$$F = \frac{F_S^Z}{\pi} \frac{(1 + 2.14\varepsilon)}{\varepsilon^{1/2}} \quad (\varepsilon \geq 1) \quad (1)$$

$$F^S = 2\pi r\gamma \sin \theta \cos \left( \frac{\pi}{2} - \alpha + \theta \right) \quad (2)$$

$$\gamma_{AP} - \gamma_{BP} = \gamma \cos \alpha \quad (3)$$

where A and B refer to grains at each side of the grain boundary;  $\gamma$  is the boundary surface tension, containing two particle/surface tensions  $\gamma_{AP}$  and  $\gamma_{BP}$ ;  $\theta$  is the bypass angle and  $\gamma_{AP} - \gamma_{BP} = \gamma \cos \alpha$ ;  $\varepsilon$  is the aspect (ratio between major axis 'b' and minor axis 'a') of the ellipsoidal particle;  $F^S$  is the dragging force from a spherical particle of the same volume [15]. For the same nanoparticle, there were two cases for the interaction (case 1 and case 2 shown in Fig. 4 c): in case 1, the dragging force increased with the aspect; in case 2, the dragging force decreased with the aspect. In this research, the interaction between the nanoparticle and grain boundary was similar to case 1, resulting in relatively lower dragging force. According to the Fig. 4 (b), this direction was nearly parallel to the close-packed  $(0001)_{\text{hcp-Zr}}$  planes, but angled from the close-packed plane of the  $\text{Zr}_3\text{Ge}$  nanoparticle. Thus, B-type HCP-FCC phase transformation was preferentially activated.

#### Data availability

The raw/processed data required to reproduce these findings cannot be shared at this time as the data also forms part of an ongoing study.



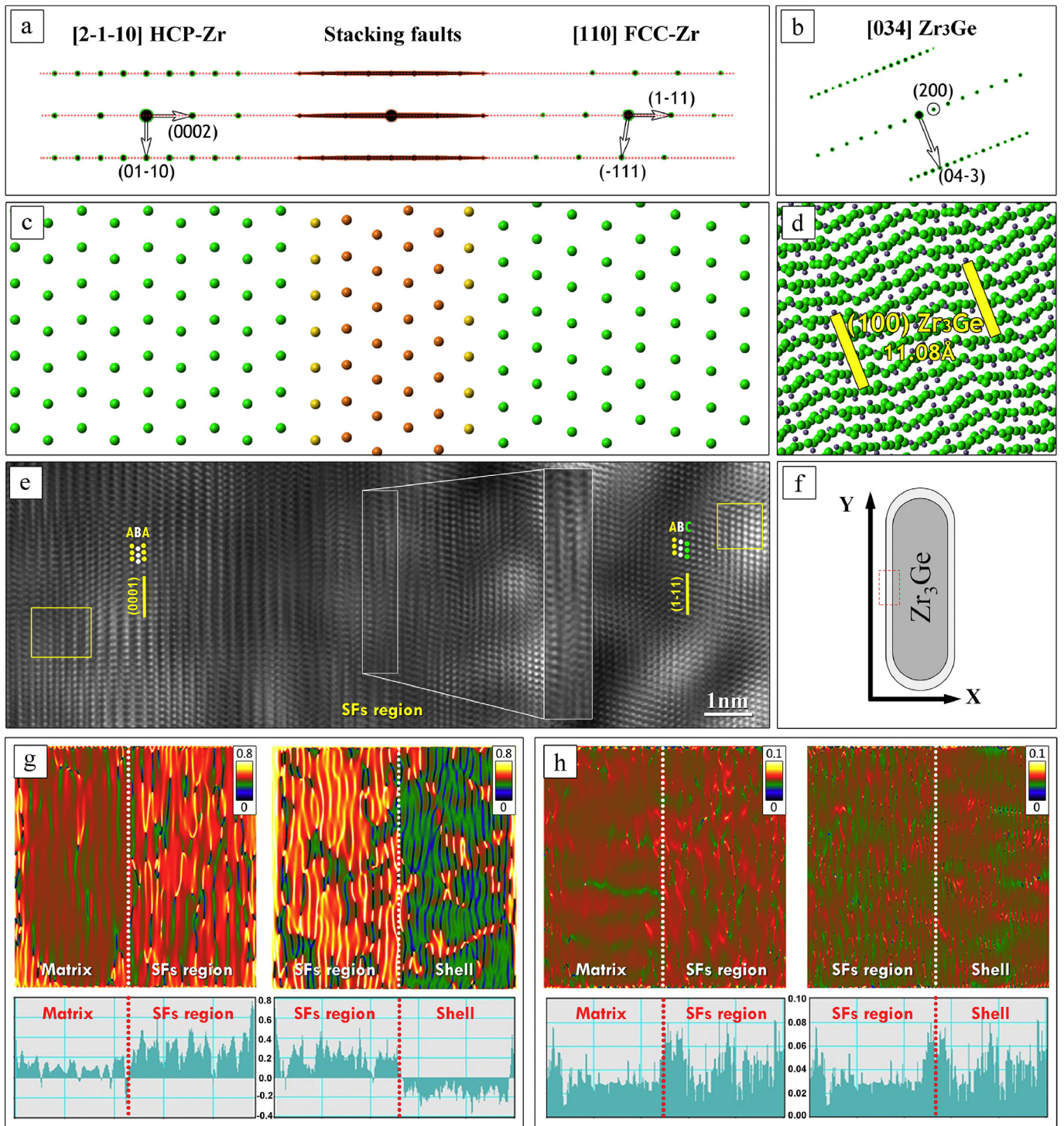


**Fig. 3.** Atomic configurations, HR-TEM images and GPA analysis for the interface region of the core-shell structured precipitate viewed along  $[2\bar{1}\bar{1}0]_{\text{HCP-Zr}}$ . (a-b) Diffraction patterns of the matrix, stacking faults region, shell structure and  $\text{Zr}_3\text{Ge}$  phase; (c-d) Atomic configurations of the matrix, stacking faults (SFs) region, shell structure and  $\text{Zr}_3\text{Ge}$  phase; (e) FFT filtered HR-TEM micrograph of the region containing the matrix, stacking faults region and shell structure; (f) The macro coordinates of the figure; (g)  $\epsilon_{xx}$  mapping and horizontal linescans of the region containing the matrix, stacking faults region and shell structure; (h)  $\epsilon_{yy}$  mapping and horizontal linescans of the region containing the matrix, stacking faults region and shell structure.

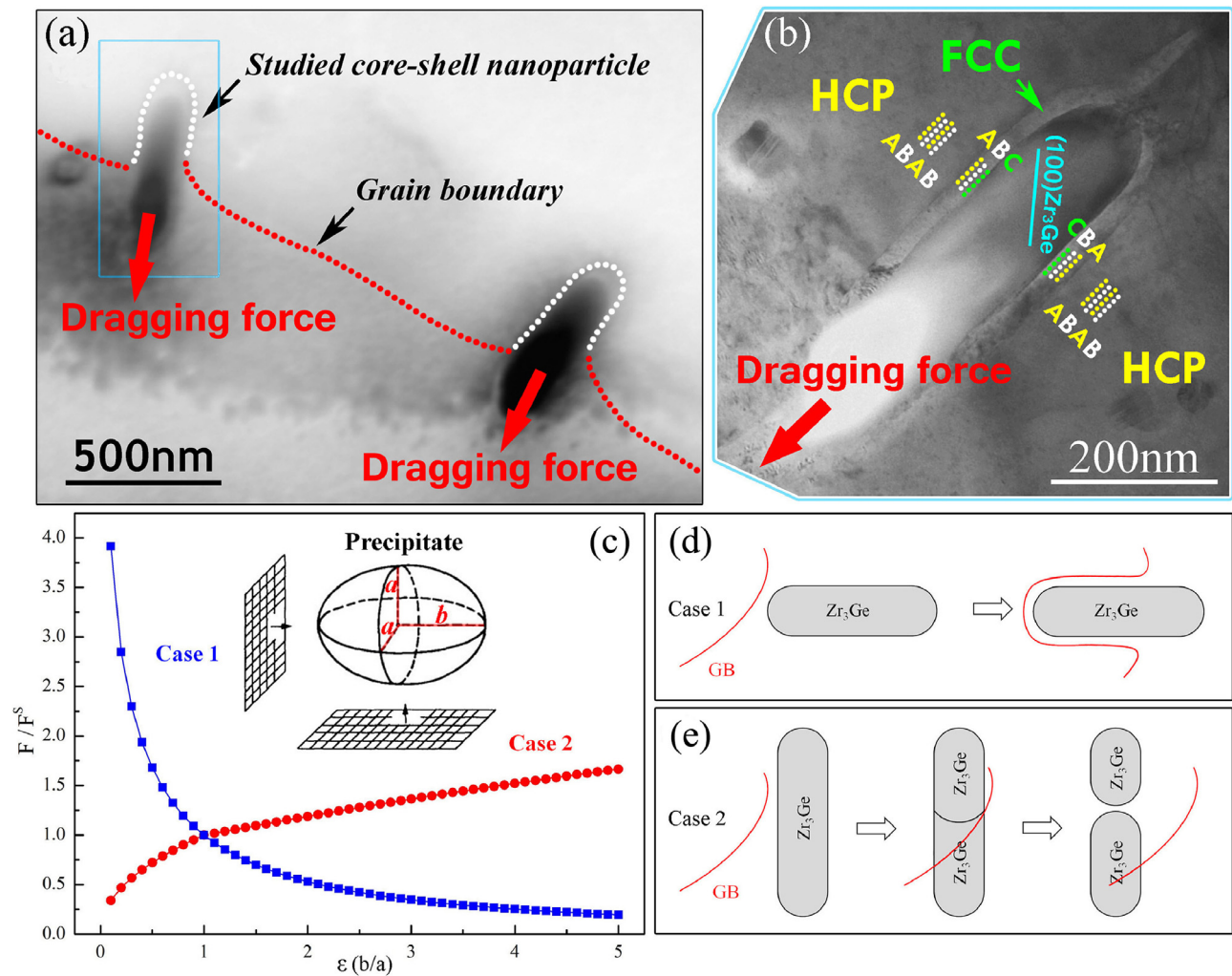


**Fig. 4.** Formation mechanism of the core-shell structured precipitates. (a) Schematic diagram showing the interaction between grain boundary and precipitates; (b) Relationship between the core-shell structured precipitate crystallography and the dragging force; (c) Dragging force as a function of  $\varepsilon$  in two cases; (d, e) Schematic diagram showing the interaction between precipitate and GB in Case 1 and 2, correspondingly.

## Declaration of Competing Interest

There are no interests to declare.

## Supplementary materials

Supplementary material associated with this article can be found, in the online version, at doi:[10.1016/j.scriptamat.2020.03.061](https://doi.org/10.1016/j.scriptamat.2020.03.061).

## References

- [1] F.W. Gayle, J.B.V. Sande, Scripta Mater. 18 (1984) 473–478.
- [2] V. Radmilovic, A. Tolley, E.A. Marquis, M.D. Russell, Z. Lee, U. Dahmen, Scripta Mater. 58 (2008) 529–532.
- [3] W. Nasim, S. Yazdi, R. Santamarta, J. Malik, D. Erdeniz, B. Mansoor, D.N. Seidman, D.C. Dunand, I. Karaman, J. Mater. Sci. 54 (2019) 1857–1871.
- [4] M.E. Krug, A. Werber, D.C. Dunand, D.N. Seidman, Acta Mater. 58 (2010) 134–145.
- [5] H. Zhao, M. Song, S. Ni, S. Shao, J. Wang, X. Liao, Acta Mater. 131 (2017) 271–279.
- [6] X. Zheng, M. Gong, T. Xiong, H. Ge, L. Yang, Y. Zhou, S. Zheng, J. Wang, X. Ma, Scripta Mater. 162 (2019) 326–330.
- [7] H. Zhao, X. Hu, M. Song, S. Ni, Scripta Mater. 132 (2017) 63–67.
- [8] J.X. Yang, H.L. Zhao, H.R. Gong, M. Song, Q.Q. Ren, Sci. Rep. 8 (2018) 1992–2000.
- [9] H.C. Wu, A. Kumar, J. Wang, X.F. Bi, C.N. Tomé, Z. Zhang, S.X. Mao, Sci. Rep. 6 (2016) 24370–24377.
- [10] D.H. Hong, T.W. Lee, S.H. Lim, W.Y. Kim, S.K. Hwang, Scripta Mater. 69 (2013) 405–408.
- [11] Hengl Zhao, Min Song, Song Ni, Shuai Shao, Jian Wang, Xiaozhou Liao, Acta Materialia 131 (2017) 271–279.
- [12] M.J. Hytch, E. Snoeck, R. Kilaas, Ultramicroscopy 74 (1998) 131–146.
- [13] Binglun Yin, Zhaoxuan Wu, W.A. Curtin, Acta Mater. 123 (2017) 223–234.
- [14] C.Z. Liu, G.P. Li, F.S. Yuan, F.Z. Han, Y.D. Zhang, H.F. Gu, Nanoscale 10 (2018) 2249–2254.
- [15] E. Nes, N. Ryum, O. Hunderi, Acta Mater. 33 (1985) 11–22.